Matter

Article

Radiation-triggered superfluorescent scintillation in quantum-ordered perovskite nanocrystal superlattices

Graphical abstract

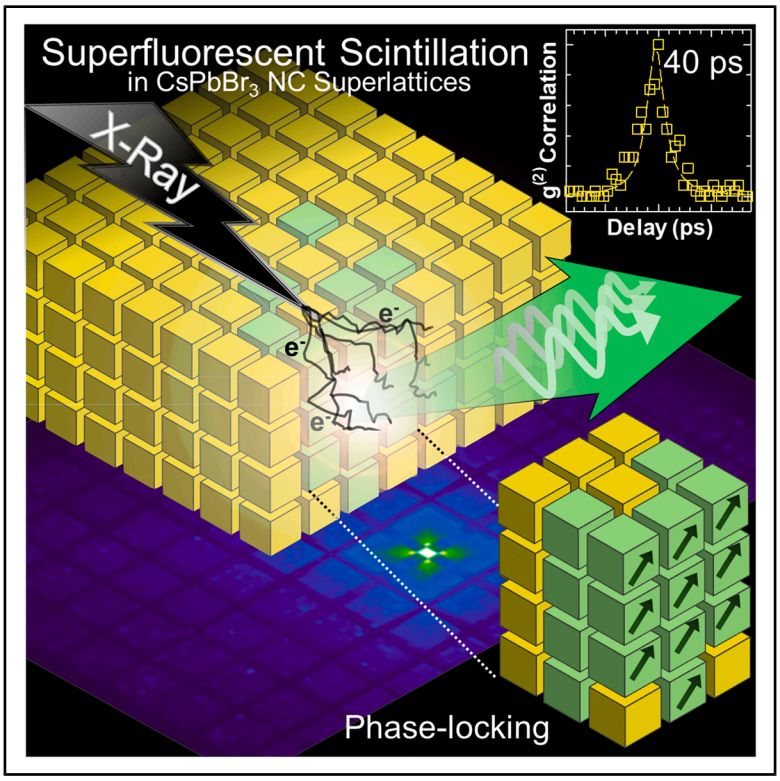

Highlights

- Superfluorescence is observed for the first time under ionizing radiation
- Perovskite nanocrystal superlattices enable ~40 ps scintillation lifetimes
- Ionization cascades can seed coherent many-body optical emission
- Reabsorption-free scintillation via collective quantum states

Authors

Matteo L. Zaffalon, Andrea Fratelli, Taras V. Sekh, ..., Luca Gironi, Maksym V. Kovalenko, Sergio Brovelli

Correspondence

mvkovalenko@ethz.ch (M.V.K.), sergio.brovelli@unimib.it (S.B.)

In brief

Nanostructured scintillators offer new ways to control how ionizing radiation is converted into light. This work shows that X-rays can trigger superfluorescence in perovskite nanocrystal superlattices, activating collective emission rather than incoherent recombination. The resulting scintillation is ultrafast, coherent, and highly efficient, with a large Stokes shift that suppresses the long-standing issue of reabsorption in dense nanocrystal assemblies. These findings establish quantum scintillation as a new regime, enabling access to coherent optical observables under ionizing radiation.

Zaffalon et al., 2026, Matter 9, 102659
April 1, 2026
https://doi.org/10.1016/j.matt.2026.102659

CellPress

Matter

CellPress
OPEN ACCESS

Article

Radiation-triggered superfluorescent scintillation in quantum-ordered perovskite nanocrystal superlattices

Matteo L. Zaffalon,[1,2] Andrea Fratelli,[1,3] Taras V. Sekh,[4] Emanuele Mazzola,[2,5] Francesco Carulli,[1] Francesco Bruni,[1,2] Maryna I. Bodnarchuk,[4] Francesco Meinardi,[1] Luca Gironi,[2,5] Maksym V. Kovalenko,[4,*] and Sergio Brovelli[1,2,6,*]

[1]Dipartimento di Scienza dei Materiali, Università degli Studi di Milano-Bicocca, via R. Cozzi 55, Milano, Italy
[2]INFN - Sezione di Milano-Bicocca, Milano, Italy
[3]Nanochemistry, Istituto Italiano di Tecnologia, via Morego 30, Genova, Italy
[4]Department of Chemistry and Applied Bioscience, ETH Zürich, Zürich, Switzerland; Laboratory for Thin Films and Photovoltaics and Laboratory for Transport at Nanoscale Interfaces, Empa – Swiss Federal Laboratories for Materials Science and Technology, Dübendorf, Switzerland
[5]Dipartimento di Fisica, Università degli Studi di Milano-Bicocca, Piazza della Scienza 3, Milano, Italy
[6]Lead contact
*Correspondence: mvkovalenko@ethz.ch (M.V.K.), sergio.brovelli@unimib.it (S.B.)
https://doi.org/10.1016/j.matt.2026.102659

PROGRESS AND POTENTIAL A long-standing challenge in scintillating materials is the difficulty of achieving fast timing response without compromising light yield. In many established scintillator platforms, faster emission is commonly obtained through intentional quenching strategies that shorten the decay at the expense of radiative efficiency. While widely used in molecular and single-crystal emitters to mitigate pile-up, this approach does not intrinsically improve timing resolution, as gains in emission dynamics are offset by reduced photon statistics. Direct-bandgap semiconductor nanomaterials offer a fundamentally different perspective, as they can in principle sustain much faster radiative decay than cross-luminescent and rare-earth-doped wide-bandgap scintillating crystals. However, their practical extension to thick, dense scintillators remains limited by strong self-absorption, which penalizes light transport and extraction in the bulk geometries required for efficient stopping of ionizing radiation. Here, we demonstrate a route beyond these limitations by exploiting collective quantum emission in long-range-ordered $CsPbBr_3$ nanocrystal superlattices assembled via controlled evaporation of colloidal solutions. We report the first observation of superfluorescence triggered by ionizing radiation, showing that stochastic ionization cascades can initiate coherent many-body states whose emission is radiatively accelerated beyond the giant oscillator strength regime of weakly confined individual nanocrystals. Importantly, this cooperative channel does not trade speed for efficiency; instead, coherence enhances the radiative rate while maintaining, and effectively boosting, emission efficiency by funneling excitation into a collective radiative mode with no corresponding ground-state absorption. As a result, ultrafast scintillation lifetimes ($\tau \approx 40$ ps) are achieved together with a large Stokes shift (>90 meV) below ~100 K. This intrinsic spectral separation enables dense nanocrystal assemblies to operate without reabsorption losses, a key requirement for scalable semiconductor scintillators. More broadly, these results indicate that scintillation under ionizing radiation can be shaped by engineered collective coherence rather than treated as an empirically fixed response, outlining a pathway toward quantum scintillators in which new coherence-based optical observables become accessible.

SUMMARY

Superfluorescence is a cooperative emission phenomenon arising from the coherent coupling of excited dipoles and has historically been observed only under optical excitation in carefully engineered quantum systems. Here, we report the first observation of superfluorescence triggered by ionizing radiation in lead-halide perovskite nanocrystal (NC) superlattices. Using $CsPbBr_3$ NC assemblies with long-range structural and electronic order, we show that secondary electrons generated by high-energy photons can induce intense cooperative emission bursts with an unprecedented scintillation lifetime of ~40 ps, defining a new class of

coherent scintillating metamaterials. Side-by-side optical and scintillation measurements reveal a direct analogy between ionizing and intense optical excitation, both producing high excitonic densities that drive superfluorescent emission at mild, technologically accessible cryogenic temperatures. The finding that stochastic ionization cascades can seed coherent many-body optical responses with radiatively accelerated luminescence and large Stokes shifts establishes a pathway toward ultrafast, reabsorption-free, quantum-ordered scintillators for next-generation radiation detectors.

INTRODUCTION

Ultrafast detection of ionizing radiation underpins modern medical imaging,[1] high-energy physics (HEP),[2–4] nuclear security,[5] and space instrumentation.[6] Despite more than half a century of optimization in crystal growth, dopant chemistry, and polymer design, virtually every commercial scintillator still channels the deposited energy into incoherent, stochastic recombination of charge carriers. In both high-Z inorganic crystals and organic plastics, the light yield (LY; defined as the number of emitted photons per unit of deposited energy), timing profile, and photon statistics are ultimately determined by the stochastic capture and recombination of localized charge carriers via disorder- or phonon-mediated pathways. These fundamental limitations impair the time-of-flight resolution in positron emission tomography (PET) scanners and the vertex reconstruction accuracy in HEP detectors. They also prevent the implementation of quantum-based readout strategies, such as those currently employed in quantum communication[7] and sensing,[8] as well as the deliberate tuning of scintillation properties by engineering many-body electronic states to enhance radiative rates, shape emission waveforms, shift spectra away from self-absorption, or control photon-number statistics.

In principle, collective coherent phenomena like superfluorescence (SF)[9,10] could enable this kind of quantum control by producing ultrafast (few-picosecond), high-brightness, coherent photon bursts. However, to date, SF has only been observed under optical pumping and has never been demonstrated in a scintillator exposed to ionizing radiation. The demonstration of SF under ionizing radiation would not only expand the fundamental understanding of collective light-matter interactions but also aligns with a growing interest in quantum-based radiation detection technologies for achieving enhanced control and information extraction from ionizing events.[8,11] In high-energy physics, such approaches could offer access to new observables and improved resolution of particle dynamics. More broadly, they may open up transformative opportunities in fields where speed, sensitivity, and miniaturization are key technological drivers.

A route beyond this structural bottleneck emerges from lead halide perovskite (LHP) nanocrystals (NCs),[12–14] particularly in the fully inorganic form $CsPbX_3$ (where X is either Cl, Br or I), that combine: (1) scalable[15,16] and low-cost fabrication, (2) the high-interaction cross-sections typical of high-Z inorganic scintillators[2,17,18]; and (3) exceptional defect tolerance and radiation hardness.[19,20] Individual LHP NCs exhibit ultrafast sub-nanosecond scintillation[21–25] driven by the recombination of multiexcitons formed under ionizing excitation[26–29] (as similarly observed in chalcogenide NCs[30–32]), which is further enhanced and accelerated under mild cryogenic conditions by the formation of giant transition dipoles (giant oscillator strength [GOS]) delocalized over the entire NC volume.[33,34] GOS causes a dramatic increase in the radiative recombination rate of both single and multiexcitons, while simultaneously boosting the efficiency of the emission process to its fully radiative limit (see sketch in Figure 1A). The result is scintillation radiative lifetimes as short as ~200 ps, with near-unity yield from isolated NCs, a highly desirable feature for fast-timing applications.[34]

A particularly powerful asset of LHP NCs for realizing the quantum-scintillation regime is their propensity to self-assemble into highly ordered structures known as superlattices (SLs). A high degree of monodispersity and shape uniformity of LHP NCs, offered through the latest synthetic advancements,[35–37] allowed the production of various single-component NC SLs[38–41] as well as multicomponent NC SLs containing different NC types.[42–45] Among semiconductor NCs, three-dimensional (3D) $CsPbBr_3$ NC SLs were the first to exhibit SF,[38,40,41,46] a phenomenon previously observed in a limited number of non-colloidal systems.[9,10] NC SLs thus emerge as a desirable platform for harnessing SF for real-world applications, owing to the broad know-how in their lattice engineering, facile patterning, scalability, and integration.[47]

In NC-SLs, SF arises from the spontaneous phase-locking of individual resonant NC transition dipoles[38,41,48] (see Figure 1A), a phenomenon facilitated by the size selection occurring during the SL formation process.[39,49,50] This phase-locking leads to the emergence of a macroscopic correlated state with energy lower than the band-edge exciton of isolated NCs, whose oscillator strength scales with the number of coupled NCs,[46,51] N. The decay of this correlated state, confined within a sub-wavelength volume, results in delayed photon bursts where both emission intensity and decay rates scale as N^2 and N, respectively.[38,41,48,52] In combination with the intra-NC GOS effect, the delayed formation and decay of these inter-NC coupled states in SLs lead to the emergence of spectrally narrower emission features with picosecond-fast decay times red-shifted by up to ~90 meV from the excitonic absorption of uncoupled NCs and without concurrent ground-state absorption, thus improving the potential for their use in high-precision detection systems.

This unique property of LHP SLs, particularly among inorganic colloidal nanostructures, has already been proposed for quantum information[53] and lasing[54,55] applications. Demonstrating such coherent emission under ionizing excitation would mark a paradigm shift: the scintillator becomes an active, many-body quantum system whose response can be engineered rather than empirically accepted. Designed in this way, reabsorption-free, picosecond-fast nanoscintillators could potentially be integrated into more complex "metascintillator" architectures, combining bulk scintillator crystal layers with nanocrystal-based systems to enhance sensitivity and spectroscopic capabilities for high-energy detection.[56]

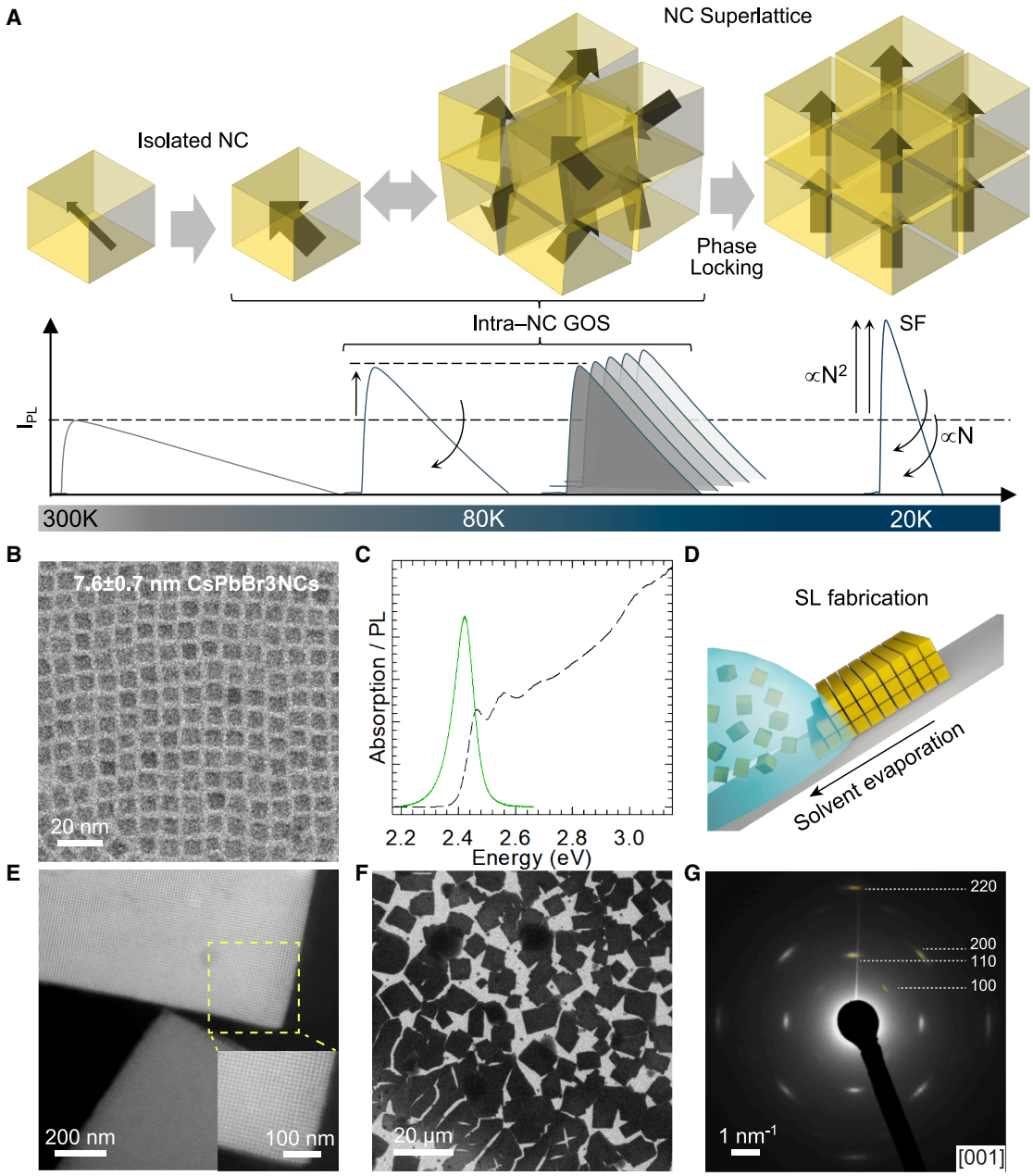

Figure 1. $CsPbBr_3$ nanocrystal superlattices

(A) Sketch showing the progressive emergence of cooperative processes in isolated NCs and in NC SLs at cryogenic temperatures, leading to acceleration of the radiative dynamics and enhancement of the luminescence. The "intra-NC" giant oscillator strength (GOS) effects, both in isolated NCs and in assembled NC superlattices, build up below room temperature, resulting in faster single emitting dipoles with near unity quantum yield. At lower temperatures, quantum phase-locking of excited states within the coherence volume of a NC SL produces an SF photon burst whose intensity and decay rate scale proportionally to the number of coupled dipoles, *N*.

(B) TEM image of starting cubic $CsPbBr_3$ NCs with an edge length of 7.6 ± 0.7 nm.

(C) Optical absorption (black line) and PL spectra (green line) of the $CsPbBr_3$ NC colloidal solution in toluene.

(D) Schematic illustration of SL fabrication by means of a drying-mediated approach, whereby the NC colloid is slowly evaporated over a tilted support, e.g., a TEM grid or SiN_x membrane.

(E) Low-magnification dark-field STEM image of two neighboring SL domains with (inset) dark-field STEM image of the area outlined with a dashed yellow line, demonstrating highly ordered NCs in simple cubic (*sc*) packing.

(F) Low-magnification TEM image of $CsPbBr_3$ NC SLs deposited on SiN_x membrane, displaying extended SL domains with an average area of *ca.* 100 μm^2.

(G) Wide-angle electron diffraction (WAED) pattern of a $[001]_{SL}$-oriented SL domain, with reflections corresponding to preferential orientation marked with yellow. The sharp reflections highlight the orientation uniformity of SL domains.

Despite the potential and early-stage efforts,[57] SF under ionizing radiation has not yet been experimentally demonstrated. Furthermore, arranging $CsPbBr_3$ NCs into two-dimensional (2D) SLs may significantly influence in-plane collective interactions by reducing the coupling dimensionality from 3D networks to 2D sheets, possibly leading to enhanced anisotropic coherent effects and further tuning of the scintillation response.

In this paper, we present the first experimental evidence of SF under ionizing radiation from 2D-like self-assembled superlattices of 7.6 nm $CsPbBr_3$ NCs. The SLs are characterized by a high degree of ordering and extended domain dimensions, as manifested by electron microscopy and electron diffraction studies. Photoluminescence (PL) measurements confirm superfluorescent behavior in such SLs at cryogenic temperatures, characterized by a narrow, red-shifted emission peak with a radiative lifetime as short as 40 ps. This is accompanied by a significant increase in emission intensity that saturates below 30 K, consistent with previous optical studies.[58,59] X-ray-excited radioluminescence (RL) experiments on the same SL show that SF is the dominant emission pathway even under ionization conditions, marking the first instance of SF-driven scintillation. Importantly, optical spectroscopy experiments as a function of excitation fluence, together with time resolved scintillation measurements, reveal that ionizing excitation induces SF at high cryogenic temperatures (80–100 K) similar to what can be achieved with high-fluence optical excitation, with a scintillation lifetime as fast as ~40 ps. As a result, over 80% of the scintillation photons originate from SF due to the high exciton density (within the decay time) created by ionizing radiation, despite the restriction of the coherence domain due to dynamic thermal disorder, which makes the SF-driven scintillation process technologically accessible. At the same time, because of the build-up time required for the formation of the correlated SF state, the optical absorption spectrum of the SL is dominated by the uncoupled domains (absorbing at higher energy with respect to the SF), resulting in no spectral overlap between the SF emission and the absorption edge and consequent absence of reabsorption losses. To gain further insights into the interaction mechanisms between ionizing radiation and the NCs within the SL, we complement our experimental observations with Monte Carlo simulations using the Geant4 toolkit.[74–76] These simulations were designed to replicate the geometry and composition of the SLs under investigation, allowing to estimate the spatial distribution of the energy deposited by incoming radiation. We thus modeled individual cubic SLs composed of $CsPbBr_3$ NCs, with nanometric resolution that reflects the actual arrangement and spacing of the NCs. By simulating both electrons and X-rays, we evaluated how energy is deposited across the lattice and how this energy distribution evolves depending on the radiation type and energy.

These results open new avenues for the development of ultrafast reabsorption-free scintillator metasolids, which hold potential for time-of-flight radiation detection technologies in both medical imaging and high-energy physics, where their ability to deliver fast, precise timing and high resolution can lead to significant advancements in radiation detection and imaging capabilities.

RESULTS AND DISCUSSION

A high degree of monodispersity and shape uniformity of SL building blocks is an essential prerequisite for the fabrication of long-range ordered SLs,[60] enabling reliable experimental study. To achieve this, $CsPbBr_3$ NCs were synthesized by means of a facile, room temperature approach assisted by trioctylphosphine oxide (TOPO) and diisooctylphosphinic acid (DOPA), which act as weakly coordinating ligands facilitating NC growth.[37] To stabilize the NCs in colloidal solution and promote their self-assembly, the labile TOPO and DOPA ligands were exchanged for stronger binding ligands. Specifically, the crude solution was first treated with a mixture of oleyl amine (OLAm) and oleic acid (OLA), followed by the addition of didodecyldimethylammonium bromide (DDAB) to improve the NCs' environmental stability.[40,61,62] The synthesis yielded highly monodisperse 7.6 ± 0.7 nm $CsPbBr_3$ NCs with a sharp cubic shape, as evident from transmission electron microscopy (TEM) imaging (Figures 1B and S1). The absorption spectrum of the NC colloidal solution exhibits multiple exciton transitions (Figure 1C), characteristic for the employed synthesis,[37] whereas the narrow NC size dispersion is reflected in a PL full width at half maximum (FWHM) of 16.7 nm.

As SF measurements require highly ordered SLs with extended domain sizes, we selected a facile drying-mediated approach on a tilted support as a method for SL fabrication[63] (Figure 1D). Unlike the deposition of 3D SLs, this method facilitates the directional alignment of SL domains on the substrate, i.e., NCs within different SL domains exhibit uniform preferential orientation. Besides, with this drying-mediated approach, the SL deposition is enabled on various substrates, including TEM grids or silicon nitride (SiN_x) membranes, using nonpolar solvents compatible with $CsPbBr_3$ NCs.[42,45]

Owing to the NCs' sharp cubic shape, self-assembly of 7.6 nm $CsPbBr_3$ NCs resulted in the formation of 2D SLs with simple cubic (*sc*) packing,[64] as confirmed by dark-field scanning transmission electron microscopy (DF-STEM) imaging (Figure 1E), consistent with previous reports on similarly sized $CsPbBr_3$ NC assemblies.[38,40] The resulting extended 2D-like SLs exhibited distinct domains with a high degree of positional and orientational NC ordering across the substrate. On transparent SiN_x membranes, individual SL domains extended over areas exceeding 100 μm^2, with a substrate coverage of ~60% (Figure 1F). In between the SL domains, few NCs were observed, i.e., the majority of NCs was located within the SL structure. The wide-angle electron diffraction (WAED) pattern displays intense, sharp sets of 100, 110, 200, and 220 reflections, indicating preferential orientation of NCs along the $[001]_{SL}$ direction (Figure 1G; subscript "SL" denotes sets of equivalent SL directions).

Prior to the scintillation measurements, we performed time- and spectrally resolved PL measurements as a function of temperature to study the emission mechanism of this new class of SLs and to verify that they exhibit SF similar to those produced by other methods reported in the literature.[38,59,65,66] Specifically, as previously observed, the characteristic signatures of SF in $CsPbBr_3$ NC SL are the delayed emergence of a low-energy emission due to coupled NCs (~60 meV below the PL from uncoupled NCs), with lifetime gradually decreasing with decreasing

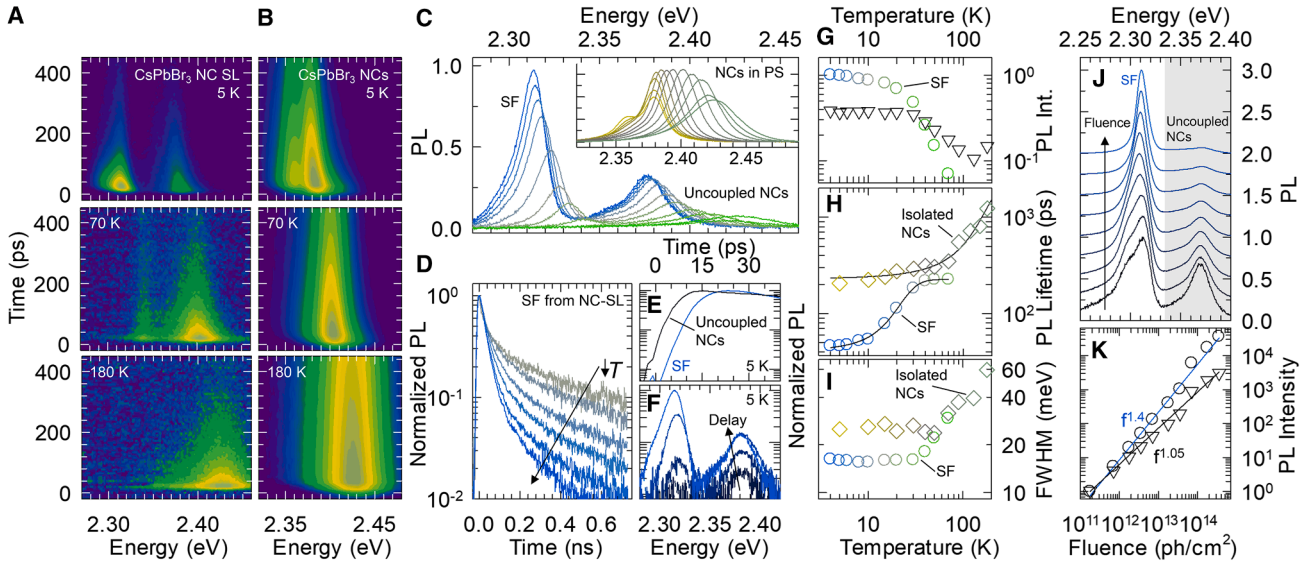

Figure 2. Optically excited SF from $CsPbBr_3$ NC superlattices

(A and B) Contour plots of spectrally and time-resolved luminescence at controlled temperature (5, 70, and 180 K from top to bottom) of (A) $CsPbBr_3$ SL and (B) isolated $CsPbBr_3$ NCs dispersed in polystyrene.

(C) PL spectra of $CsPbBr_3$ NC SL measured in the 5–180 K temperature range. Inset: PL spectra of isolated NCs in polystyrene. The spectra have been normalized at the corresponding maximum at 5 K.

(D) Normalized PL decay traces of the superfluorescence (SF) component from $CsPbBr_3$ NC SL in the 5–40 K temperature range.

(E) PL rise signals of the SF (blue) and uncoupled (black) components extracted from (A).

(F) PL spectra extracted from the (A) at progressively longer delay times (0, 3, 10, and 24 ps).

(G) Intensity of the SF component (circles) from NC SL and corresponding PL from isolated NCs (triangles) as function of temperature.

(H) PL lifetimes of SF component (circles) and of isolated NCs in polystyrene (diamonds) at controlled temperature. The lines are a guide for the eye.

(I) Emission spectral width—expressed as FWHM—of the SF component in (C) (circles) and of the PL for isolated NCs in polystyrene (diamonds).

(J) PL spectra of $CsPbBr_3$ NC SL at 5 K at increasing excitation fluence. The spectra have been normalized to their maxima and vertically shifted for clarity.

(K) Integrated PL intensity from (L) for the SF (circles) and uncoupled NC PL (triangles) components as a function of excitation photon fluence. The same temperature color scheme applies throughout the figure.

temperature (down to ~40 ps) and fluence scaling of SF intensity (I_{SF}) approaching the quadratic theoretical limit ($I_{SF} \sim f^{1.5}$ in Rainò et al.[38]). Figure 2A shows the contour plots of PL(E,t) collected by a streak camera (resolution <10 ps) at T = 180, 70, and 5 K under low optical excitation such that the average exciton population was <0.1 exciton per NC. For comparison, Figure 2B shows the analogous contour plots of a disordered film of the same NCs dispersed in a polystyrene matrix. The complete set of spectra and their decay curves within the investigated temperature range is shown in Figures 2C, 2D, and S2. The respective parameters of integrated PL intensity (I_{PL}), lifetime, and linewidth (FWHM) are quantified in Figures 2G–2I. Figures 2E and 2F show a detail of the time rise of SF and PL intensity at 5 K from uncoupled NCs in the SL and the corresponding emission spectra at increasing delay times (0–24 ps) extracted from Figure 1A. At 180 K, both samples exhibit a single PL peak at 2.43 eV, characteristic of isolated $CsPbBr_3$ NCs, which intensifies and red-shifts with decreasing temperature as a result of bandgap renormalization[67] and suppression of non-radiative decay channels. At the same time, the film of isolated NCs shows the shortening of the luminescence lifetime due to the gradual build-up of the oscillator strength of individual NCs, i.e., the appearance of GOS, approaching saturation at about 70 K, in agreement with recent reports.[34,68] The emissive component from isolated NCs of the SL follows the same trend, but with a basically constant lifetime at about 100 ps (not shown), due to the dominant effect of dynamic quenching by the copper substrate of the TEM grid on which it is placed. More importantly, at about 90 K, the SL shows the onset of a second, narrower emission peak at about 2.33 eV, shifted by ~60 meV from the corresponding emission of isolated NCs at 2.39 eV. This narrow emission is consistent with the SF reported for similar SLs[38] and is due to collective emission from coupled NCs in higher-order local domains. Consistently, reducing the thermal disorder counteracting phase coupling by further lowering the temperature causes its strong enhancement to become the largely dominant emission, accelerating to about 40 ps lifetime and narrowing (Figures 2G–2I). In contrast, lowering the temperature below 80 K has little effect on the intensity and dynamics of the decoupled emission of both SL and polystyrene NC film, consistent with the saturation of the oscillator strength and emission yield.

Also consistent with previous results,[38] the SF intensity shows a delay time of ~6 ps from the corresponding uncoupled PL due to the formation of the correlated SF state, as highlighted by the respective decay traces and spectra collected at increasing times after the excitation pulse shown in Figures 2E and 2F. As will be shown later in this work (*vide infra*), the fact that the superfluorescent state does not exist in the ground state but is formed

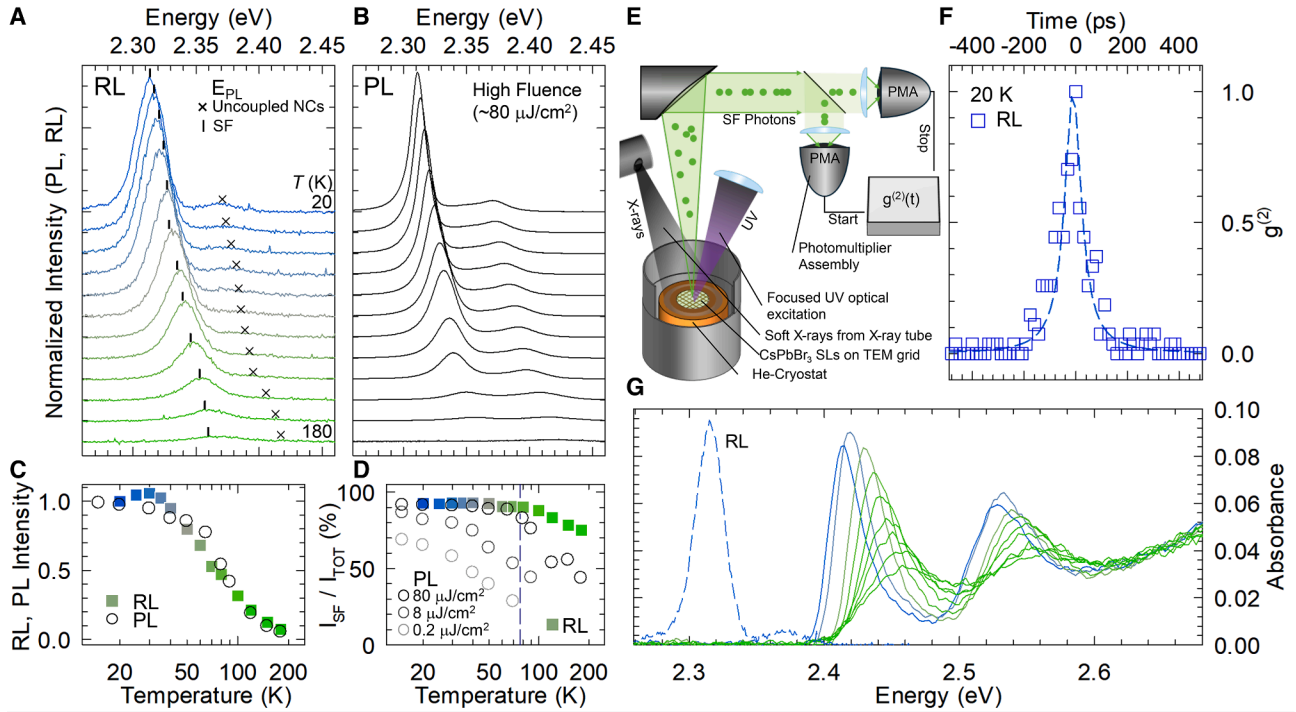

Figure 3. SF under ionizing excitation

(A) Radioluminescence (RL) spectra of $CsPbBr_3$ SLs at controlled temperatures from 180 to 20 K (from bottom to top). The spectra have been normalized to the spectrum maximum at 20 K and vertically shifted for clarity. The vertical ticks and crosses correspond to the spectral positions (E_{PL}) of SF and isolated emissions, respectively, from the corresponding PL spectra under high fluence excitation, as shown in (B).

(C) Normalized integrated PL (circles) and RL (squares) intensity as a function of temperature as extracted from (A) and (B).

(D) Relative intensity of the SF component (expressed as I_{SF}/I_{total}) as a function of temperature from RL (squares) and PL (circles) measurements at increasing fluences (~0.2, 8, and 80 μJ/cm^2). The vertical dashed line corresponds to the technologically relevant liquid nitrogen temperature.

(E) Schematic illustration of the cross-correlation setup in the Hanbury Brown and Twiss configuration, together with a sketch of sample's excitation (X-rays or UV light) and SF light collection within a He-cryostat.

(F) Second-order RL (squares) correlation function measured for $CsPbBr_3$ NC SLs at 20 K along with the best fit with a Lorentzian function (blue line) featuring an FWHM of 80 ps.

(G) A set of representative optical absorption spectra at decreasing temperatures (from 290 to 20 K, from green to blue) for $CsPbBr_3$ SLs. The corresponding RL spectrum at 20 K is shown for reference as a dashed line (not in scale).

gradually over time is advantageous for the realization of superfluorescent scintillators because it separates the optical absorption due to NCs before their coupling from the SF due to coupled NCs. Taken together, these spectroscopic signatures confirm the collective emission in SL of $CsPbBr_3$ NCs and the gradual increase in the number of coupled NCs at progressively lower temperatures. Further confirming this attribution, measurements of PL at 5 K as a function of excitation fluence, f (Figures 2J and 2K), show a linear trend ($I_{PL} \sim f^{1.05}$) for the emission from isolated NCs and proportional to $f^{1.4}$ for the SF component, for which a theoretical quadratic limit trend in the absence of non-radiative losses is predicted in agreement with Rainò et al.[38]

After confirming the SF process and validating this class of SLs as a model system for the study of SF scintillation, we performed temperature-dependent RL measurements in the 20–180 K range using a tungsten cathode X-ray tube as the excitation source, which produces a continuous bremsstrahlung spectrum with a mean energy of 9.6 keV. The collected spectra are shown in Figure 3A. At 20 K, the RL spectrum displays two distinct components whose lineshapes are independent of the X-ray energy (see Figure S3) and spectrally match the band-edge emission of isolated NCs and the coupled SF state discussed above, with the latter accounting for more than 92% of the total RL signal. This confirms that, as in previously studied disordered NC films,[29] the interaction with ionizing radiation in $CsPbBr_3$ SLs is intrinsically equivalent to high-fluence optical excitation, implying that, in RL measurements, the energy deposited by X-ray photons alone is sufficient to trigger and sustain collective phenomena, making SF the dominant scintillation mechanism. In this regard, it is important to note that ionizing interaction generates multiple excitons in individual NCs following a carrier multiplication process,[26,30] which is particularly advantageous for the SF regime because the collective oscillator strength of coupled NCs increases with the exciton density within the coherence domain. As shown in Figure S4, the scintillation of isolated NCs shows an average excitonic population $\langle N \rangle \sim 1.5$ in agreement with previous reports.[26] Consistently, the RL shows the same spectral evolution (see markers in Figure 3A), as well as similar intensity trends and relative intensity contribution between the SF and isolated NC components,

as the temperature-dependent PL spectra collected under high fluence excitation (~80 μJ/cm^2, i.e., ~1.8 × 10^{14} ph/cm^2; Figure 3B), selected to match the ⟨N⟩ produced under X-rays. The corresponding integrated PL and RL intensities, along with the branching ratio between the coupled and uncoupled emission, are quantified in Figures 3C and 3D, respectively (the complete set of PL spectra as a function of fluence is reported in Figure S5). These figures highlight a particularly relevant aspect of the parallelism between high irradiance optical and ionizing excitation, namely that both lead to essentially instantaneous formation of high excitation densities within the coherence domain of SL. As a result, SF scintillation under X-rays (as well as its optical counterpart) is observed even at high temperatures despite increasing dynamical disorder. Specifically, the SF component consistently accounts for more than 70% of the total RL signal in the experimental temperature range and shows promising performance even at liquid nitrogen temperatures, a mild cryogenic regime that is already technologically accessible. For example, at ~80 K, the relative contribution of the SF component has already approached its maximum of ~90%, while the total RL intensity is only reduced by a factor of two compared to 20 K. Further confirmation that the coupled SF regime is driven by long-range dipole ordering in superlattices, rather than by the high exciton densities generated under ionizing radiation, comes from RL measurements of a disordered film, whose spectra in Figure S6 follow the same temperature evolution as the corresponding PL in Figure 2 and show no trace of a red-shifted collective band at lower energies, despite a deposited energy per NC comparable to that of the SL sample. A crucial aspect of the SF regime is the radiative acceleration of emission dynamics, which improves scintillation timing. To measure scintillation kinetics below ~100 ps, as expected based on PL dynamics in Figures 2D and 2H, we performed two-photon cross-correlation measurements[69] under continuous-wave X-ray excitation (see sketch in Figure 3E). This configuration is necessary for time-resolved RL because the pulse width of pulsed X-ray tubes typically exceeds 120 ps.[70] Figure 3F reports the measured $g^{(2)}$ curve at 20 K showing a positive peak that decreases to zero at increasing delay times, as expected from photon bunches produced by SF. From analyzing the $g^{(2)}$ kinetics, we obtained a scintillation lifetime of ~40 ps (see methods section for details), confirming the potential of SF scintillation for fast timing applications. To the best of our knowledge, this is the fastest scintillation time ever reported under ionizing radiation. Only Cherenkov-based processes are intrinsically faster,[71,72] yet their extremely low and highly fluctuating photon yields (typically <20 photons per γ-event in PET scanners for $Bi_4Ge_3O_{12}$ [BGO] crystals) limit their practical use as time taggers to enhancing the timing performance of the scintillating host material in which they are generated, provided that advanced pulse-shaping and filtering algorithms are employed.[73] Finally, the close match between the scintillation and high-fluence optically excited PL enables us to study the temperature- and fluence-dependence of SF in greater detail using the time-correlated single-photon counting technique. Figure S7 shows the decay curves at 50 K as a function of femtosecond laser excitation fluence, as well as the decay curves at ⟨N⟩ ~1.5 as a function of temperature, together with the corresponding effective lifetimes. The complete set of PL decays and the detailed analysis of the SF dynamics, including the fit convoluted with the detector's response time, are presented in Figure S8. Consistent with the expected SF trend,[38–41] decreasing the temperature and increasing the fluence results in accelerated decay kinetics compared to those observed at low fluence in Figure 2. This is due to the simultaneous increase in the average excitonic population per NC (i.e., activation of the multiexcitonic regime) and increased number of excited NCs within the coherence domain.

Overall, the spectral and timing behavior provides the first evidence that $CsPbBr_3$ SLs can operate as cryogenic scintillators in which the RL originates predominantly from a coupled SF state, resulting in emission that is further red-shifted by ~60 meV from isolated NCs and radiatively accelerated with lifetimes that can reach a few tens of ps, depending on the number of coupled emitters. These are the key requirements for a dense, ultrafast scintillator capable of emitting intense photon bursts spectrally decoupled from the host (emitter) matrix. Stopping high-energy photons, such as those used in medical imaging, requires scintillators a few centimeters thick with negligible optical losses due to self-absorption to maximize light output to the detector. To further support this application, Figure 3G shows the temperature evolution of the optical absorption profile of $CsPbBr_3$ SLs deposited on an ultra-thin transparent SiN_x membrane. At room temperature, the high monodispersity of the NCs allows to resolve the first two excitonic transitions at 2.46 and 2.56 eV, in excellent agreement with previous reports on highly monodisperse colloidal solutions of NCs with similar size.[37,74] As temperature decreases, both transitions shift to lower energy, following thermal expansion of the NCs lattice, and increase in intensity due to the onset of intra-NC GOS. At 20 K, the lowest 1S transition reaches ~2.41 eV. Notably, the corresponding RL spectrum shows a residual RL from uncoupled NCs at 2.37 eV, consistent with the typical Stokes shift of $CsPbBr_3$ NCs,[75] and a dominant SF peak at 2.31 eV, setting the overall spectral shift between the SF scintillation and the SL absorption edge up to 100 meV, which essentially completely hinders reabsorption.

To gain deeper insight into the mechanisms underlying energy deposition in NC SLs, we performed Monte Carlo simulations using the Geant4 toolkit, starting from a representative SL geometry composed of 7.6 nm $CsPbBr_3$ NCs separated by 1.4 nm OLAm ligands. Figure 4A illustrates the case of a cubic SL with ~100 nm edge length (containing 1,728 NCs), irradiated by a uniform flux of X-rays matching the spectral distribution of the source used in Figure 3. The projection of the energy deposited by external X-rays in the XY plane is shown in Figure S9. These simulations reveal how incident radiation interacts with the SL's architecture and provide a spatially resolved map of energy deposition within the lattice. Notably, energy is absorbed predominantly in the NCs rather than the surrounding OLAm, indicating the dominant role of the perovskite domains in radiation-matter interaction.

To further investigate how energy spreads following a primary interaction, we simulated the generation of energetic electrons at the center of the cubic SL and tracked their energy-loss trajectories (Figure 4B). While this setup is not fully representative of physical X-ray interaction—since X-rays do

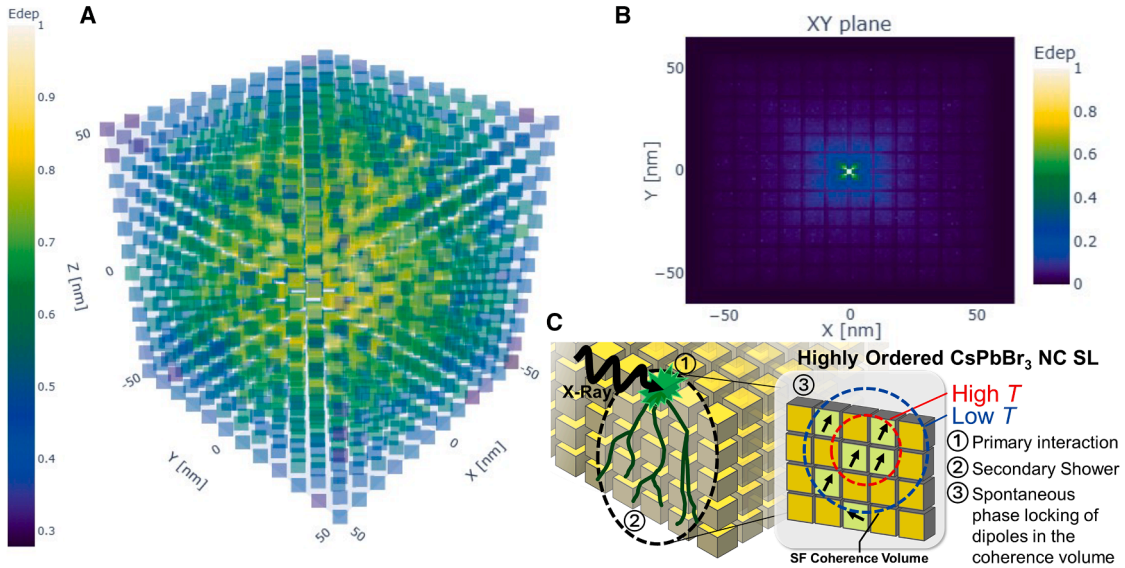

Figure 4. Monte Carlo simulation of energy deposition in nanocrystal SLs

(A) Three-dimensional rendering of a simulated cubic SL composed of 1728 $CsPbBr_3$ NCs regularly arranged and embedded in a surrounding OLAm matrix. Each NC is color coded based on the energy deposited (normalized over the maximum released) per incident X-ray (excitation source outside the SL), illustrating the spatial distribution of the energy within the lattice.

(B) Orthogonal projections onto the plane XY of the energy deposited (normalized over the maximum released) for the case of internally generated photoelectrons in the center of the same cubic SL represented in (A).

(C) Schematic representation of the superfluorescent scintillation mechanism in highly ordered SL made of cubic $CsPbBr_3$ NCs and its dependence on temperature.

not typically generate electrons at the SL center—it offers valuable insight into local energy propagation. Unlike diluted solutions or polymeric NC dispersions, where most of the energy dissipates into the inert matrix,[76] the densely packed SL architecture promotes localized energy retention, enhancing local exciton generation and radiative recombination.[77,78] Although these detailed simulations are informative, they become computationally expensive as the number of NCs increases. For realistic SLs containing ~20 million NCs, explicitly modeling each particle becomes unpractical. A feasible solution is to adopt a simplified approach in which the SL is approximated as a homogeneous medium with equivalent mass fractions of $CsPbBr_3$ and OLAm. We validated this method by comparing the energy deposited in the mixed-volume model with that of explicit NC simulations (Figure S10), finding that the difference becomes negligible for NC counts above $\sim 10^6$. Based on this validation, we simulated a flat SL of ~100 μm^2 surface area and 141 nm thickness, corresponding to a realistic lattice of ~20 million NCs. The resulting mean deposited energy per interacting X-ray photon was 3.97 keV. Combined with the quantitative RL measurements shown in Figure 3A, this enables us to estimate the LY of our SLs under X-ray excitation, yielding LY = 64,000 ± 20,000 photons/MeV at 20 K (see methods for details). This value is higher than that of standard $CsPbBr_3$ NC films (~10,000–15,000 photons/MeV) and is consistent with a scintillation process that is largely radiative. Nevertheless, the theoretical maximum LY for $CsPbBr_3$ remains ~160,000 photons/MeV, indicating that photo-charge-to-exciton conversion in the SL is still incomplete.[79,80]

It is important to note that the LY estimation should be interpreted with caution, as accurate experimental measurement of the deposited energy is currently not feasible. Nevertheless, the RL system was calibrated assuming Lambertian emission from the sample, which represents a conservative (lower-bound) assumption for the collection geometry compared to fully isotropic emission. This simulation also enables an instructive comparison between the exciton densities generated in an SL by ionizing and optical excitation. Under our experimental conditions, the X-ray photon flux per SL is sufficiently low, and the relaxation dynamics sufficiently fast, that interaction events can be regarded as independent single-photon excitations, directly comparable to individual laser pulses at low repletion rate. Combining the SL dimensions, the lateral extent of the energy-deposition volume obtained from the Geant4 simulations, and the mean energy deposited per interacting X-ray photon (see supplemental information for details), we estimate that a single X-ray photon generates an exciton population of ~400 within the relevant volume, comparable to that produced by each optical pulse under the excitation conditions described for Figure 3B.

In conclusion, we successfully fabricated macroscopically two-dimensional SLs from highly monodisperse 7.6 nm $CsPbBr_3$ NCs, stabilized with OLAm/OLA/DDAB ligands that promote controlled self-assembly. Transmission electron microscopy and electron diffraction analyses revealed highly ordered, orientationally locked NCs arranged in a cubic lattice. Remarkably, the resulting SLs exhibited large, continuous domains (~100 μm^2) with high areal coverage on TEM grids and SiN_x membranes. We employed

these $CsPbBr_3$ SLs as a model platform to investigate collective optical phenomena under ionizing radiation. We demonstrated that under X-ray excitation, the RL of the SLs is dominated by SF, accounting for over 90% of the total emission with lifetimes as fast as ~40 ps at 20 K. This ultrafast response persisted with minimal degradation up to and beyond 80 K. These findings indicate that ionizing excitation can drive the system into a collective emission regime, establishing SF as the primary scintillation mechanism in this class of hybrid metamaterials. Complementary temperature-dependent optical absorption measurements revealed clear signatures of the giant oscillator strength effect at the band edge and confirmed the absence of spectral overlap between the SF emission and the absorption edge, indicating negligible self-absorption losses. To understand how energy is deposited in the SL under high-energy irradiation, we performed Monte Carlo simulations using Geant4, modeling the NC lattice embedded in an OLAm matrix. Simulations showed that the majority of the total energy deposited by secondary interactions is found within closed-packed NCs along thin tracks consistent with the spatial scales of collective coupling. Taken together, our results establish $CsPbBr_3$ SLs as a new generation of solution-processable scintillators, in which collective radiative phenomena govern the response under both optical and ionizing excitation. This paves the way for ultrafast detection architectures based on coherently emitting NC assemblies with minimal reabsorption losses and fundamentally new mechanisms for signal generation and processing.

METHODS

Synthesis of $CsPbBr_3$ nanocrystals and SL growth

$CsPbBr_3$ NCs were fabricated employing the adopted procedure from Akkerman et al.[37] $PbBr_2$-TOPO stock solution (0.04 M) was prepared by dissolving $PbBr_2$ (1 mmol, 367 mg, Sigma-Aldrich) and trioctylphosphine oxide (TOPO, 5 mmol, 1.933 g, Strem) into octane (5 mL, Roth) at 110°C in a 40 mL vial. After all $PbBr_2$ dissolved, the solution was allowed to cool down to room temperature, and hexane (20 mL) was added. The stock solution was then filtered with 0.2 μm PTFE filter.

Cs-DOPA stock solution (0.02 M) was prepared by dissolving Cs_2CO_3 (0.3 mmol, 100 mg, Sigma-Aldrich) and diisooctylphosphinic acid (DOPA, 3.15 mmol, 1 mL, Sigma-Aldrich) into octane (2 mL, Roth) at 110°C in a 40 mL vial. After all Cs_2CO_3 dissolved, the solution was allowed to cool down to room temperature, and hexane (27 mL) was added. The stock solution was then filtered with 0.2 μm PTFE filter.

Oleyl amine (OLAm, Strem, distilled) and oleic acid (OLA, Sigma-Aldrich) ligand solution was prepared by mixing OLAm (0.33 mL, 1 mmol) and OLA (0.316 mL, 1 mmol) in anhydrous hexane (2.5 mL).

Didodecyldimethylammonium bromide (DDAB) solution (0.215 M) was prepared by dissolving DDAB (Sigma-Aldrich, 0.3 g, 0.65 mmol) in anhydrous toluene (3 mL, Sigma-Aldrich).

Synthesis of 7.6 nm $CsPbBr_3$ NCs

In a 25 mL round-bottom flask, $PbBr_2$-TOPO stock solution (1.5 mL) was combined with hexane (1 mL) upon vigorous stirring (1,400 rpm). Then Cs-DOPA stock solution (0.75 mL) was injected, and after stirring for 90 s, OLAm and OLA ligand solution (1 mL) was added. The solution was allowed to stir for 60 s, and DDAB (30 μL) was injected. NC colloid was then concentrated with a rotary evaporator and washed with anhydrous ethyl acetate (EtOAc, 1:1 v/v). NCs were redispersed in anhydrous toluene and stored inside the glovebox.

Fabrication of $CsPbBr_3$ NC SLs

$CsPbBr_3$ NC SLs were prepared employing drying-mediated approach (Figure 1D). TEM grids (F/C-coated, Ted Pella, with the Formvar layer removed by immersing the grid in toluene for 10 s) or SiN_x membranes (Agar Scientific, Norcada) were employed as the substrates. The NC colloid (5–10 μL, 2 μM) was placed along with 15 μL anhydrous toluene in a 2 mL vial with a solid support inside. The vial was then tilted in a vacuum chamber (pressure ~0.5 bar, room temperature), where the solvent slowly evaporated overnight.

Microscopy characterization

TEM and STEM images, as well as WAED patterns, were collected with a JEOL JEM 2200FS electron microscope operating at an accelerating voltage of 200 kV. Image analysis was performed using ImageJ.

Optical spectroscopy

The optical absorption spectra, also measured as a function of temperature, were collected using a Lambda 950 spectrophotometer (PerkinElmer) equipped with an integrating sphere and coupled with a closed-circuit He cryostat. For low-fluence ultrafast time-resolved PL (trPL) measurements, the samples excited with frequency-doubled Ti:sapphire laser (E_{exc} = 3.06 eV, pulse duration ~150 fs, repetition rate ~76 MHz), collecting the emitted light with a Hamamatsu streak camera (time resolution <10 ps). For fluence-dependent PL measurements—both continuous wave (cw) and time-resolved—the samples were excited with an amplified laser from Ultrafast Systems operated at 15 kHz, producing ~260 fs pulses at 3.06 eV when coupled an independently tunable optical parametric amplifier from the same supplier. The emitted light was collected with a Horiba Triax 190 monochromator (grating 1,200 lines/mm) coupled with a cooled Horiba Sincerity CCD for steady state PL and a Cornerstone 260 1/4 m VIS-NIR monochromator coupled with a PicoQuant PMA Hybrid Series-07 and a PicoHarp 300 time-correlated single photon counting unit. All the PL measurements were performed inside a closed-circuit cryostat operated in evaporated He atmosphere at ~10 mbar.

Intensity cross-correlation measurement

Two-photon cross-correlation measurement was conducted using a standard Hanbury Brown and Twiss configuration with two matched PMA Hybrid Series-07 single-photon detectors. The intensity correlation function ($g^{(2)}$) was generated using the two detectors as start and stop triggers for a PicoHarp 300 time-tagger. Negative correlation times were probed thanks to an electronic delay set for one of the two channels. The correlator's resolution is estimated to be ~70 ps—FWHM—assuming a ~50 ps spread time for each detector. The SF dynamics have been calculated from the fitted FWHM according to the following:

$$\tau_{SF} \approx \sqrt{FWHM^2_{Meas} - FWHM^2_{Instr}}.$$

Radioluminescence spectroscopy

The cryogenic radioluminescence measurements were performed with a closed cycle He cryostat exciting the sample with unfiltered X-rays produced by a Philips PW2274 X-ray tube with a tungsten target, equipped with a beryllium window, and operated at 20 kV to produce a continuous X-ray spectrum through bremsstrahlung effect. The scintillation light spectra were collected using a liquid-nitrogen-cooled, back-illuminated, UV-enhanced CCD detector (Jobin Yvon Symphony II), coupled to a monochromator (Jobin Yvon Triax 180) with a 600 lines/mm grating. The time response of scintillation light was measured using a pulsed X-ray source composed by a 405 nm ps-pulsed laser (Edinburgh Instruments, EPL-405) hitting the photocathode of an X-ray tube from Hamamatsu (model N5084) set at 40 kV. The scintillation was collected using a MicroHR spectrometer from Horiba (equipped with a 150 lines/mm grating) coupled with a PicoQuant PMA Hybrid Series-07 and a PicoHarp 300 for time-correlated single photon counting (time resolution ~120 ps).

Light yield estimation

The light yield (LY) is defined as the ratio between the number of emitted photons and the energy deposited in the scintillator, typically expressed in MeV.

$$\mathrm{LY} = \frac{N_{\mathrm{ph}}}{E_{\mathrm{deposited}}} \left[\mathrm{photons\ MeV}^{-1}\right]$$

To convert the CCD counts from the radioluminescence (RL) spectrum into the photon number N_{ph}, we first measured the optical detection efficiency of the setup at the SF wavelength. A continuous-wave 532 nm laser was coupled into a multimode optical fiber with a core diameter of 600 μm, chosen to match the lateral dimensions of the sample, and with a numerical aperture equal to that of the first collection optic. The power emitted from the fiber tip was measured using a calibrated power meter and converted into the number of emitted photons per second. The detection efficiency η is then calculated as the ratio between the CCD counts (when measuring the light intensity from the fiber tip under the same grating, slit, and geometrical conditions used for the RL measurement) and the photon flux at the fiber tip. The sample was modeled as a Lambertian emitter to estimate the total number of photons produced per second.

To determine the energy deposited in the scintillator, we first calculate the X-ray tube photon flux N_X (ph·cm^{-2}·s^{-1}) as:

$$N_X = \frac{D_{\mathrm{air}}}{\int \tilde{\Phi}(E)\left(\frac{\mu_{\mathrm{en}}}{\rho}(E)\right)_{Air} E\, dE}, \text{ where } \int \tilde{\Phi}(\mathrm{E})\, \mathrm{dE} = 1.$$

Here, D_{Air} (J kg^{-1}s^{-1}) is the air dose rate (measured with a calibrated ionization chamber), $\tilde{\Phi}(E)$ the X-ray photon fluence spectrum (simulated using the XMI-MSIM package[81] and normalized so that $\int \tilde{\Phi}(E)\, dE = 1$), and $\frac{\mu_{\mathrm{en}}}{\rho}(E)$, cm^2/g the mass energy-absorption coefficients of dry air (as extracted from NIST X-COM database[82]).

The number of incident X-ray photons on the sample (N_{inc}) is obtained by multiplying N_X by the illuminated sample area (A_S), i.e., $N_{inc} = N_X A_S$. The total energy deposited in the sample is then estimated from the Geant4 results as $E_D = N_{inc}\, f_I\, \langle \Delta E \rangle$, where f_I is the fraction of interacting X-rays (~1%) and $\langle \Delta E \rangle$ is ~4 keV.

RESOURCE AVAILABILITY

Lead contact

Requests for further information and resources should be directed to and will be fulfilled by the lead contact, Prof. Sergio Brovelli (sergio.brovelli@unimib.it).

Materials availability

This study did not generate new, unique reagents.

Data and code availability

All data reported in this paper will be shared by the lead contact upon reasonable request. This paper does not report original code.

ACKNOWLEDGMENTS

This work was funded by Horizon Europe EIC Pathfinder program through project 101098649 – UNICORN, by the European Union -Next Generation EU, Mission 4 Component 1 CUP H53D23004670006 and CUP H53D23004500006, and through the Italian Ministry of University and Research under PNRR—M4C2-I1.3 Project PE_00000019 "HEAL ITALIA." This research is funded and supervised by the Italian Space Agency (Agenzia Spaziale Italiana, ASI) in the framework of the Research Day "Giornate della Ricerca Spaziale" initiative through the contract ASI N. 2023-4-U.0t. This work was also supported by the Office of Naval Research under grant no. N629092512073.

AUTHOR CONTRIBUTIONS

S.B. and M.V.K. conceived this work. T.V.S. synthesized the NCs and assembled the superlattices under the supervision of M.I.B. and M.V.K. M.L.Z., A.F., F.B., and F.C. conducted the spectroscopic and scintillation experiments under the supervision of S.B. and F.M. E.M. conducted the GEANT4 simulations under the supervision of L.G. S.B., M.L.Z., and F.M. wrote the paper in consultation with all authors.

DECLARATION OF INTERESTS

The authors declare no competing interests.

SUPPLEMENTAL INFORMATION

Supplemental information can be found online at https://doi.org/10.1016/j.matt.2026.102659.

Received: September 29, 2025
Revised: November 19, 2025
Accepted: January 5, 2026
Published: March 4, 2026

REFERENCES

1. Lecoq, P., Morel, C., Prior, J.O., Visvikis, D., Gundacker, S., Auffray, E., Križan, P., Turtos, R.M., Thers, D., Charbon, E., et al. (2020). Roadmap toward the 10 ps time-of-flight PET challenge. Phys. Med. Biol. *65*, 21RM01. https://doi.org/10.1088/1361-6560/ab9500.
2. Fabjan, C.W., and Gianotti, F. (2003). Calorimetry for particle physics. Rev. Mod. Phys. *75*, 1243–1286. https://doi.org/10.1103/RevModPhys.75.1243.
3. van Blaaderen, J.J., van Aarle, C., Leibold, D., Dorenbos, P., and Schaart, D.R. (2025). Guidelines for the Selection of Scintillators for Indirect Photon-Counting X-ray Detectors. Chem. Mater. *37*, 1716–1740. https://doi.org/10.1021/acs.chemmater.4c03437.

4. Lecoq, P., Auffray, E., Brunner, S., Hillemanns, H., Jarron, P., Knapitsch, A., Meyer, T., and Powolny, F. (2010). Factors Influencing Time Resolution of Scintillators and Ways to Improve Them. Ieee T Nucl Sci *57*, 2411–2416. https://doi.org/10.1109/Tns.2010.2049860.

5. Partridge, T., Astolfo, A., Shankar, S.S., Vittoria, F.A., Endrizzi, M., Arridge, S., Riley-Smith, T., Haig, I.G., Bate, D., and Olivo, A. (2022). Enhanced detection of threat materials by dark-field x-ray imaging combined with deep neural networks. Nat. Commun. *13*, 4651. https://doi.org/10.1038/s41467-022-32402-0.

6. Kim, C., Lee, W., Melis, A., Elmughrabi, A., Lee, K., Park, C., and Yeom, J.-Y. (2021). A Review of Inorganic Scintillation Crystals for Extreme Environments. Crystals *11*, 669. https://doi.org/10.3390/cryst11060669.

7. Luo, W., Cao, L., Shi, Y., Wan, L., Zhang, H., Li, S., Chen, G., Li, Y., Li, S., Wang, Y., et al. (2023). Recent progress in quantum photonic chips for quantum communication and internet. Light Sci. Appl. *12*, 175. https://doi.org/10.1038/s41377-023-01173-8.

8. Bass, S.D., and Doser, M. (2024). Quantum sensing for particle physics. Nat. Rev. Phys. *6*, 329–339. https://doi.org/10.1038/s42254-024-00714-3.

9. Skribanowitz, N., Herman, I.P., MacGillivray, J.C., and Feld, M.S. (1973). Observation of Dicke Superradiance in Optically Pumped HF Gas. Phys. Rev. Lett. *30*, 309–312. https://doi.org/10.1103/PhysRevLett.30.309.

10. Timothy Noe Ii, G., Kim, J.-H., Lee, J., Wang, Y., Wójcik, A.K., McGill, S.A., Reitze, D.H., Belyanin, A.A., and Kono, J. (2012). Giant superfluorescent bursts from a semiconductor magneto-plasma. Nat. Phys. *8*, 219–224. https://doi.org/10.1038/nphys2207.

11. Di Meglio, A., Doser, M., Frisch, B., Grabowska, D.M., Pierini, M., and Vallecorsa, S. (2021). CERN Quantum Technology Initiative Strategy and Roadmap (1.0_Rev2). Zenodo. http://doi.org/10.5281/zenodo/5571809.

12. Anand, A., Zaffalon, M.L., Erroi, A., Cova, F., Carulli, F., and Brovelli, S. (2024). Advances in Perovskite Nanocrystals and Nanocomposites for Scintillation Applications. ACS Energy Lett. *9*, 1261–1287. https://doi.org/10.1021/acsenergylett.3c02763.

13. Wibowo, A., Sheikh, M.A.K., Diguna, L.J., Ananda, M.B., Marsudi, M.A., Arramel, A., Zeng, S., Wong, L.J., and Birowosuto, M.D. (2023). Development and challenges in perovskite scintillators for high-resolution imaging and timing applications. Commun. Mater. *4*, 21. https://doi.org/10.1038/s43246-023-00348-5.

14. Martinazzoli, L., Nargelas, S., Boháček, P., Calá, R., Dušek, M., Rohlíček, J., Tamulaitis, G., Auffray, E., and Nikl, M. (2022). Compositional engineering of multicomponent garnet scintillators: towards an ultra-accelerated scintillation response. Mater. Adv. *3*, 6842–6852. https://doi.org/10.1039/D2MA00626J.

15. Akkerman, Q.A., Gandini, M., Di Stasio, F., Rastogi, P., Palazon, F., Bertoni, G., Ball, J.M., Prato, M., Petrozza, A., and Manna, L. (2016). Strongly emissive perovskite nanocrystal inks for high-voltage solar cells. Nat. Energy *2*, 16194. https://doi.org/10.1038/nenergy.2016.194.

16. Calora, M., Carulli, F., Vanni, N., Giuri, A., Ferrari, E., Masino, M., Lazzarini, L., Rossi, F., Accorsi, G., Moliterni, A., et al. (2025). Defect-Mediated Scintillation in Fully Inorganic Perovskites via Water-Induced 0D/3D Phase Modulation. Adv. Funct. Mater. *2025*, e12571. https://doi.org/10.1002/adfm.202512571.

17. Dujardin, C., Auffray, E., Bourret-Courchesne, E., Dorenbos, P., Lecoq, P., Nikl, M., Vasil'ev, A.N., Yoshikawa, A., and Zhu, R.-Y. (2018). Needs, Trends, and Advances in Inorganic Scintillators. Ieee T Nucl Sci *65*, 1977–1997. https://doi.org/10.1109/TNS.2018.2840160.

18. Chen, Q., Wu, J., Ou, X., Huang, B., Almutlaq, J., Zhumekenov, A.A., Guan, X., Han, S., Liang, L., Yi, Z., et al. (2018). All-inorganic perovskite nanocrystal scintillators. Nature *561*, 88–93. https://doi.org/10.1038/s41586-018-0451-1.

19. Huang, H., Bodnarchuk, M.I., Kershaw, S.V., Kovalenko, M.V., and Rogach, A.L. (2017). Lead Halide Perovskite Nanocrystals in the Research Spotlight: Stability and Defect Tolerance. ACS Energy Lett. *2*, 2071–2083. https://doi.org/10.1021/acsenergylett.7b00547.

20. Zaffalon, M.L., Cova, F., Liu, M., Cemmi, A., Di Sarcina, I., Rossi, F., Carulli, F., Erroi, A., Rodà, C., Perego, J., et al. (2022). Extreme γ-ray radiation hardness and high scintillation yield in perovskite nanocrystals. Nat. Photonics *16*, 860–868. https://doi.org/10.1038/s41566-022-01103-x.

21. Děcká, K., Pagano, F., Frank, I., Kratochwil, N., Mihóková, E., Auffray, E., and Čuba, V. (2022). Timing performance of lead halide perovskite nanoscintillators embedded in a polystyrene matrix. J. Mater. Chem. C Mater. *10*, 12836–12843. https://doi.org/10.1039/d2tc02060b.

22. Tomanová, K., Suchá, A., Mihóková, E., Procházková, L., Jakubec, I., Turtos, R.M., Gundacker, S., Auffray, E., and Cuba, V. (2020). CsPbBr3 Thin Films on LYSO:Ce Substrates. Ieee T Nucl Sci *67*, 933–938. https://doi.org/10.1109/Tns.2020.2978581.

23. Děcká, K., Král, J., Hájek, F., Průša, P., Babin, V., Mihóková, E., and Čuba, V. (2022). Scintillation Response Enhancement in Nanocrystalline Lead Halide Perovskite Thin Films on Scintillating Wafers. Nanomaterials *12*, 10014. https://doi.org/10.3390/nano12010014.

24. O'Neill, J., Braddock, I., Crean, C., Ghosh, J., Masteghin, M., Richards, S., Wilson, M., and Sellin, P. (2023). Development and characterisation of caesium lead halide perovskite nanocomposite scintillators for X-ray detection. Front. Phys. *10*, 1046589. https://doi.org/10.3389/fphy.2022.1046589.

25. Pagano, F., Král, J., Decká, K., Pizzichemi, M., Mihóková, E., Cuba, V., and Auffray, E. (2024). Nanocrystalline Lead Halide Perovskites to Boost Time-of-Flight Performance of Medical Imaging Detectors. Adv Mater Interfaces *11*, 2300659. https://doi.org/10.1002/admi.202300659.

26. Fratelli, A., Zaffalon, M.L., Mazzola, E., Dirin, D.N., Cherniukh, I., Otero-Martínez, C., Salomoni, M., Carulli, F., Rossi, F., Meinardi, F., et al. (2025). Size-Dependent Multiexciton Dynamics Governs Scintillation From Perovskite Quantum Dots. Adv. Mater. *37*, e2413182. https://doi.org/10.1002/adma.202413182.

27. Carulli, F., Erroi, A., Bruni, F., Zaffalon, M.L., Liu, M., Pascazio, R., El Adel, A., Catalano, F., Cemmi, A., Di Sarcina, I., et al. (2024). Surface Modified CsPbBr3 Nanocrystals Enable Free Radical Thermal Polymerization of Efficient Ultrafast Polystyrenic Nanocomposite Scintillators. ACS Energy Lett. *10*, 12–21. https://doi.org/10.1021/acsenergylett.4c02711.

28. Erroi, A., Carulli, F., Cova, F., Frank, I., Zaffalon, M.L., Llusar, J., Mecca, S., Cemmi, A., Di Sarcina, I., Rossi, F., et al. (2024). Ultrafast Nanocomposite Scintillators Based on Cd-Enhanced CsPbCl3 Nanocrystals in Polymer Matrix. ACS Energy Lett. *9*, 2333–2342. https://doi.org/10.1021/acsenergylett.4c00778.

29. Erroi, A., Mecca, S., Zaffalon, M.L., Frank, I., Carulli, F., Cemmi, A., Di Sarcina, I., Debellis, D., Rossi, F., Cova, F., et al. (2023). Ultrafast and Radiation-Hard Lead Halide Perovskite Nanocomposite Scintillators. ACS Energy Lett. *8*, 3883–3894. https://doi.org/10.1021/acsenergylett.3c01396.

30. Turtos, R.M., Gundacker, S., Polovitsyn, A., Christodoulou, S., Salomoni, M., Auffray, E., Moreels, I., Lecoq, P., and Grim, J.Q. (2016). Ultrafast emission from colloidal nanocrystals under pulsed X-ray excitation. J. Instrum. *11*, P10015. https://doi.org/10.1088/1748-0221/11/10/P10015.

31. Guzelturk, B., Diroll, B.T., Cassidy, J.P., Harankahage, D., Hua, M., Lin, X.-M., Iyer, V., Schaller, R.D., Lawrie, B.J., and Zamkov, M. (2024). Bright and durable scintillation from colloidal quantum shells. Nat. Commun. *15*, 4274. https://doi.org/10.1038/s41467-024-48351-9.

32. Meng, Z., Mahler, B., Houel, J., Kulzer, F., Vasil'ev, A., and Dujardin, C. (2022). Perspective on the scintillating response of CdSe based nanoplatelets heterostructures. Mater. Adv. *3*, 8341–8350. https://doi.org/10.1039/d2ma00635a.

33. Zhu, C., Boehme, S.C., Feld, L.G., Moskalenko, A., Dirin, D.N., Mahrt, R.F., Stöferle, T., Bodnarchuk, M.I., Efros, A.L., Sercel, P.C., et al. (2024). Single-photon superradiance in individual caesium lead halide quantum dots. Nature *626*, 535–541. https://doi.org/10.1038/s41586-023-07001-8.

34. Zaffalon, M.L., Fratelli, A., Li, Z., Bruni, F., Cherniukh, I., Carulli, F., Meinardi, F., Kovalenko, M.V., Manna, L., and Brovelli, S. (2025). Ultrafast Superradiant Scintillation from Isolated Weakly Confined Perovskite

Nanocrystals. Adv. Mater. *37*, e2500846. https://doi.org/10.1002/adma.202500846.

35. Protesescu, L., Yakunin, S., Bodnarchuk, M.I., Krieg, F., Caputo, R., Hendon, C.H., Yang, R.X., Walsh, A., and Kovalenko, M.V. (2015). Nanocrystals of Cesium Lead Halide Perovskites (CsPbX(3), X = Cl, Br, and I): Novel Optoelectronic Materials Showing Bright Emission with Wide Color Gamut. Nano Lett. *15*, 3692–3696. https://doi.org/10.1021/nl5048779.
36. Dong, Y., Qiao, T., Kim, D., Parobek, D., Rossi, D., and Son, D.H. (2018). Precise Control of Quantum Confinement in Cesium Lead Halide Perovskite Quantum Dots via Thermodynamic Equilibrium. Nano Lett. *18*, 3716–3722. https://doi.org/10.1021/acs.nanolett.8b00861.
37. Akkerman, Q.A., Nguyen, T.P.T., Boehme, S.C., Montanarella, F., Dirin, D.N., Wechsler, P., Beiglböck, F., Rainò, G., Erni, R., Katan, C., et al. (2022). Controlling the nucleation and growth kinetics of lead halide perovskite quantum dots. Science *377*, 1406–1412. https://doi.org/10.1126/science.abq3616.
38. Rainò, G., Becker, M.A., Bodnarchuk, M.I., Mahrt, R.F., Kovalenko, M.V., and Stöferle, T. (2018). Superfluorescence from lead halide perovskite quantum dot superlattices. Nature *563*, 671–675. https://doi.org/10.1038/s41586-018-0683-0.
39. Boehme, S.C., Bodnarchuk, M.I., Burian, M., Bertolotti, F., Cherniukh, I., Bernasconi, C., Zhu, C., Erni, R., Amenitsch, H., Naumenko, D., et al. (2023). Strongly Confined CsPbBr3 Quantum Dots as Quantum Emitters and Building Blocks for Rhombic Superlattices. ACS Nano *17*, 2089–2100. https://doi.org/10.1021/acsnano.2c07677.
40. Kobiyama, E., Urbonas, D., Aymoz, B., Bodnarchuk, M.I., Rainò, G., Olziersky, A., Caimi, D., Sousa, M., Mahrt, R.F., Kovalenko, M.V., and Stöferle, T. (2025). Perovskite Nanocrystal Self-Assemblies in 3D Hollow Templates. ACS Nano *19*, 6748–6757. https://doi.org/10.1021/acsnano.4c07819.
41. Tang, Y., Jing, Y., Sum, T.C., Bruno, A., and Mhaisalkar, S.G. (2025). Superfluorescence in Metal Halide Perovskites. Adv. Energy Mater. *15*, 2400322. https://doi.org/10.1002/aenm.202400322.
42. Cherniukh, I., Rainò, G., Stöferle, T., Burian, M., Travesset, A., Naumenko, D., Amenitsch, H., Erni, R., Mahrt, R.F., Bodnarchuk, M.I., and Kovalenko, M.V. (2021). Perovskite-type superlattices from lead halide perovskite nanocubes. Nature *593*, 535–542. https://doi.org/10.1038/s41586-021-03492-5.
43. Cherniukh, I., Rainò, G., Sekh, T.V., Zhu, C., Shynkarenko, Y., John, R.A., Kobiyama, E., Mahrt, R.F., Stöferle, T., Erni, R., et al. (2021). Shape-Directed Co-Assembly of Lead Halide Perovskite Nanocubes with Dielectric Nanodisks into Binary Nanocrystal Superlattices. ACS Nano *15*, 16488–16500. https://doi.org/10.1021/acsnano.1c06047.
44. Cherniukh, I., Sekh, T.V., Rainò, G., Ashton, O.J., Burian, M., Travesset, A., Athanasiou, M., Manoli, A., John, R.A., Svyrydenko, M., et al. (2022). Structural Diversity in Multicomponent Nanocrystal Superlattices Comprising Lead Halide Perovskite Nanocubes. ACS Nano *16*, 7210–7232. https://doi.org/10.1021/acsnano.1c10702.
45. Sekh, T.V., Cherniukh, I., Kobiyama, E., Sheehan, T.J., Manoli, A., Zhu, C., Athanasiou, M., Sergides, M., Ortikova, O., Rossell, M.D., et al. (2024). All-Perovskite Multicomponent Nanocrystal Superlattices. ACS Nano *18*, 8423–8436. https://doi.org/10.1021/acsnano.3c13062.
46. Levy, S., Be'er, O., Shaek, S., Gorlach, A., Scharf, E., Ossia, Y., Liran, R., Cohen, K., Strassberg, R., Kaminer, I., et al. (2025). Collective Interactions of Quantum-Confined Excitons in Halide Perovskite Nanocrystal Superlattices. ACS Nano *19*, 963–971. https://doi.org/10.1021/acsnano.4c12509.
47. Bassani, C.L., van Anders, G., Banin, U., Baranov, D., Chen, Q., Dijkstra, M., Dimitriyev, M.S., Efrati, E., Faraudo, J., Gang, O., et al. (2024). Nanocrystal Assemblies: Current Advances and Open Problems. ACS Nano *18*, 14791–14840. https://doi.org/10.1021/acsnano.3c10201.
48. Dicke, R.H. (1954). Coherence in Spontaneous Radiation Processes. Phys. Rev. *93*, 99–110. https://doi.org/10.1103/PhysRev.93.99.
49. Filippi, U., Toso, S., Zaffalon, M.L., Pianetti, A., Li, Z., Marras, S., Goldoni, L., Meinardi, F., Brovelli, S., Baranov, D., and Manna, L. (2025). Cooling-Induced Order-Disorder Phase Transition in CsPbBr(3) Nanocrystal Superlattices. Adv. Mater. *37*, e2410949. https://doi.org/10.1002/adma.202410949.
50. Clark, D.E., Lumsargis, V.A., Blach, D.D., Zhu, K., Shumski, A.J., Yao, L., Chen, Q., Huang, L., and Li, C.W. (2022). Quantifying Structural Heterogeneity in Individual CsPbBr3 Quantum Dot Superlattices. Chem. Mater. *34*, 10200–10207. https://doi.org/10.1021/acs.chemmater.2c03153.
51. Rainò, G., Utzat, H., Bawendi, M.G., and Kovalenko, M.V. (2020). Superradiant emission from self-assembled light emitters: From molecules to quantum dots. MRS Bull. *45*, 841–848. https://doi.org/10.1557/mrs.2020.250.
52. Bonifacio, R., and Lugiato, L.A. (1975). Cooperative radiation processes in two-level systems: Superfluorescence. Phys. Rev. *11*, 1507–1521. https://doi.org/10.1103/PhysRevA.11.1507.
53. Zhu, J., Li, Y., Lin, X., Han, Y., and Wu, K. (2024). Coherent phenomena and dynamics of lead halide perovskite nanocrystals for quantum information technologies. Nat. Mater. *23*, 1027–1040. https://doi.org/10.1038/s41563-024-01922-z.
54. Zhong, Y., Zhou, C., Hou, L., Li, J., Xie, W., Dong, H., and Zhang, L. (2022). Ultrafast Optical Properties of Cavity-Enhanced Superfluorescence. Adv. Opt. Mater. *10*, 2102290. https://doi.org/10.1002/adom.202102290.
55. Poonia, A.K., Mondal, B., Beard, M.C., Nag, A., and Adarsh, K.V. (2024). Superfluorescence from Electron-Hole Plasma at Moderate Temperatures of 175 K. Phys. Rev. Lett. *132*, 063803. https://doi.org/10.1103/PhysRevLett.132.063803.
56. Konstantinou, G., Lecoq, P., Benlloch, J.M., and Gonzalez, A.J. (2022). Metascintillators for Ultrafast Gamma Detectors: A Review of Current State and Future Perspectives. IEEE Trans. Radiat. Plasma Med. Sci. *6*, 5–15. https://doi.org/10.1109/TRPMS.2021.3069624.
57. Katznelson, S., Levy, S., Gorlach, A., Regev, N., Birk, M., Mechel, C., Tziperman, O., Schuetz, R., Strassberg, R., Dosovitsky, G., et al. (2024). Superfluorescent scintillation from coupled perovskite quantum dots. Preprint at arXiv. https://doi.org/10.48550/arXiv.2412.21101.
58. Pashaei Adl, H., Gorji, S., Muñoz-Matutano, G., Gualdrón-Reyes, A.F., Suárez, I., Chirvony, V.S., Mora-Seró, I., and Martínez-Pastor, J.P. (2023). Superradiance Emission and Its Thermal Decoherence in Lead Halide Perovskites Superlattices. Adv. Opt. Mater. *11*, 2202497. https://doi.org/10.1002/adom.202202497.
59. Luo, L., Tang, X., Park, J., Wang, C.-W., Park, M., Khurana, M., Singh, A., Cheon, J., Belyanin, A., Sokolov, A.V., and Son, D.H. (2025). Polarized Superradiance from CsPbBr3 Quantum Dot Superlattice with Controlled Interdot Electronic Coupling. Nano Lett. *25*, 6176–6183. https://doi.org/10.1021/acs.nanolett.5c00478.
60. Boles, M.A., Engel, M., and Talapin, D.V. (2016). Self-Assembly of Colloidal Nanocrystals: From Intricate Structures to Functional Materials. Chem. Rev. *116*, 11220–11289. https://doi.org/10.1021/acs.chemrev.6b00196.
61. Stelmakh, A., Aebli, M., Baumketner, A., and Kovalenko, M.V. (2021). On the Mechanism of Alkylammonium Ligands Binding to the Surface of CsPbBr(3) Nanocrystals. Chem. Mater. *33*, 5962–5973. https://doi.org/10.1021/acs.chemmater.1c01081.
62. Bodnarchuk, M.I., Boehme, S.C., Ten Brinck, S., Bernasconi, C., Shynkarenko, Y., Krieg, F., Widmer, R., Aeschlimann, B., Günther, D., Kovalenko, M.V., and Infante, I. (2019). Rationalizing and Controlling the Surface Structure and Electronic Passivation of Cesium Lead Halide Nanocrystals. ACS Energy Lett. *4*, 63–74. https://doi.org/10.1021/acsenergylett.8b01669.
63. Bodnarchuk, M.I., Kovalenko, M.V., Heiss, W., and Talapin, D.V. (2010). Energetic and entropic contributions to self-assembly of binary

nanocrystal superlattices: temperature as the structure-directing factor. J. Am. Chem. Soc. *132*, 11967–11977. https://doi.org/10.1021/ja103083q.

64. Hallstrom, J., Cherniukh, I., Zha, X., Kovalenko, M.V., and Travesset, A. (2023). Ligand Effects in Assembly of Cubic and Spherical Nanocrystals: Applications to Packing of Perovskite Nanocubes. ACS Nano *17*, 7219–7228. https://doi.org/10.1021/acsnano.2c10079.

65. Mao, D., Chen, L., Sun, Z., Zhang, M., Shi, Z.-Y., Hu, Y., Zhang, L., Wu, J., Dong, H., Xie, W., and Xu, H. (2024). Observation of transition from superfluorescence to polariton condensation in CsPbBr3 quantum dots film. Light Sci. Appl. *13*, 34. https://doi.org/10.1038/s41377-024-01378-5.

66. Aggarwal, N., Poonia, A.K., Dirin, D.N., Cherniukh, I., Sinha, A., Waghmare, U.V., Bodnarchuk, M.I., Wüster, S., Kovalenko, M.V., and Adarsh, K.V. (2025). Room Temperature Superfluorescence from an Electron-Hole Liquid. Phys. Rev. Lett. *134*, 083801. https://doi.org/10.1103/PhysRevLett.134.083801.

67. Shibata, K., Yan, J., Hazama, Y., Chen, S., and Akiyama, H. (2020). Exciton Localization and Enhancement of the Exciton–LO Phonon Interaction in a CsPbBr3 Single Crystal. J. Phys. Chem. C *124*, 18257–18263. https://doi.org/10.1021/acs.jpcc.0c06254.

68. Zhang, B., Goldoni, L., Lambruschini, C., Moni, L., Imran, M., Pianetti, A., Pinchetti, V., Brovelli, S., De Trizio, L., and Manna, L. (2020). Stable and Size Tunable CsPbBr(3) Nanocrystals Synthesized with Oleylphosphonic Acid. Nano Lett. *20*, 8847–8853. https://doi.org/10.1021/acs.nanolett.0c03833.

69. Fox, M. (2006). Quantum Optics: An Introduction (Oxford University Press).

70. Gundacker, S., Turtos, R.M., Auffray, E., and Lecoq, P. (2018). Precise rise and decay time measurements of inorganic scintillators by means of X-ray and 511 keV excitation. Nucl Instrum Meth A *891*, 42–52. https://doi.org/10.1016/j.nima.2018.02.074.

71. Gomez-Cadenas, J.J., Benlloch-Rodríguez, J.M., and Ferrario, P. (2017). Monte Carlo study of the coincidence resolving time of a liquid xenon PET scanner, using Cherenkov radiation. J. Instrum. *12*, P08023. https://doi.org/10.1088/1748-0221/12/08/P08023.

72. Roncali, E., Kwon, S.I., Jan, S., Berg, E., and Cherry, S.R. (2019). Cerenkov light transport in scintillation crystals explained: realistic simulation with GATE. Biomed. Phys. Eng. Express *5*, 035033. https://doi.org/10.1088/2057-1976/ab0f93.

73. Kratochwil, N., Auffray, E., and Gundacker, S. (2021). Exploring Cherenkov Emission of BGO for TOF-PET. IEEE Trans. Radiat. Plasma Med. Sci. *5*, 619–629. https://doi.org/10.1109/TRPMS.2020.3030483.

74. Akkerman, Q.A. (2022). Spheroidal Cesium Lead Chloride–Bromide Quantum Dots and a Fast Determination of Their Size and Halide Content. Nano Lett. *22*, 8168–8173. https://doi.org/10.1021/acs.nanolett.2c02601.

75. Brennan, M.C., Herr, J.E., Nguyen-Beck, T.S., Zinna, J., Draguta, S., Rouvimov, S., Parkhill, J., and Kuno, M. (2017). Origin of the Size-Dependent Stokes Shift in CsPbBr3 Perovskite Nanocrystals. J. Am. Chem. Soc. *139*, 12201–12208. https://doi.org/10.1021/jacs.7b05683.

76. Bulin, A.-L., Vasil'ev, A., Belsky, A., Amans, D., Ledoux, G., and Dujardin, C. (2015). Modelling energy deposition in nanoscintillators to predict the efficiency of the X-ray-induced photodynamic effect. Nanoscale *7*, 5744–5751. https://doi.org/10.1039/C4NR07444K.

77. Zhou, X., Zaffalon, M.L., Mazzola, E., Fratelli, A., Carulli, F., Wang, C., He, M., Bruni, F., Chakraborty, S., Poletti, L., et al. (2026). Harnessing self-sensitized scintillation by supramolecular engineering of CsPbBr3 nanocrystals in dense mesoporous template nanospheres. Adv. Mater. *38* (*4*), e13469. https://doi.org/10.1002/adma.202513469.

78. Bruni, F., Chakraborty, S., Fratelli, A., El Adel, A., Llusar, J., Carulli, F., Zaffalon, M.L., Wang, C., Zabloudil, V., Auffray, E., et al. (2025). Synergistic Compatibilization of CsPbBr3 Perovskites and HfO2 Nanocrystals for Hybrid Sensitized Nanoscintillators. Adv. Funct. Mater. *2025*, e20228. https://doi.org/10.1002/adfm.202520228.

79. Robbins, D.J. (1980). On Predicting the Maximum Efficiency of Phosphor Systems Excited by Ionizing Radiation. J. Electrochem. Soc. *127*, 2694–2702. https://doi.org/10.1149/1.2129574.

80. Padilha, L.A., Stewart, J.T., Sandberg, R.L., Bae, W.K., Koh, W.-K., Pietryga, J.M., and Klimov, V.I. (2013). Carrier Multiplication in Semiconductor Nanocrystals: Influence of Size, Shape, and Composition. Acc. Chem. Res. *46*, 1261–1269. https://doi.org/10.1021/ar300228x.

81. Schoonjans, T., Solé, V.A., Vincze, L., Sanchez del Rio, M., Appel, K., and Ferrero, C. (2013). A general Monte Carlo simulation of energy-dispersive X-ray fluorescence spectrometers — Part 6. Quantification through iterative simulations. Spectrochim. Acta B Atom Spectrosc. *82*, 36–41. https://doi.org/10.1016/j.sab.2012.12.011.

82. Berger, M.J., Hubbell, J.H., Seltzer, S.M., Chang, J., Coursey, J.S., Sukumar, R., Zucker, D.S., and Olsen, K. (2010). XCOM: Photon Cross Section Database (version 1.5).